ELSEVIER

Contents lists available at ScienceDirect

# Additive Manufacturing

journal homepage: www.elsevier.com/locate/addma



# Research Paper



# Selectively doped piezoelectric ceramics with tunable piezoelectricity via suspension-enclosing projection stereolithography

Li He <sup>a,1,2</sup>, Xiao Wang <sup>b</sup>, Fan Fei <sup>a</sup>, Lei Chen <sup>c</sup>, Xuan Song <sup>a,\*</sup>

- <sup>a</sup> Department of Industrial and Systems Engineering, the University of Iowa, Iowa City, IA 52242, USA
- <sup>b</sup> School of Mechatronic Engineering, Jiangsu Normal University, Xuzhou, Jiangsu 221116, China
- <sup>c</sup> Department of Mechanical Engineering, University of Michigan-Dearborn, Dearborn, MI 48128-1491, USA

### ARTICLE INFO

#### Keywords: Stereolithography Selective doping Piezoelectricity Ceramics

#### ABSTRACT

The macroscopic piezoelectric properties of piezoelectric materials can be regulated via localized control of microstructures to introduce site-specific electric displacement vectors, but much of the current research is centered around design and manipulation of meso-scale architectural units that are inherently limited in achieving high functionality. In this study, we propose a stereolithography-based additive manufacturing (AM) strategy to spatially tune the properties of piezoelectric ceramics at a grain-microstructural scale through selectively incorporating dopants into the ceramic materials for tailoring the grain development. The effects of different doping parameters (including ceramic solid loading, dopant type, and dopant concentration) on the microstructures and properties of printed piezoelectric ceramics are investigated. The thermodynamics and kinetics of different doping additives in the dopant-ceramic interaction are experimentally and numerically studied to enable location-specific inhibition of microstructures. Our results indicate that a doping concentration of 2 wt % promoted the homogeneity of local grain growth, resulted in a higher compressive strength and lower porosity, and improved dielectric permittivity and piezoelectric voltage constant in printed piezoelectric ceramics. Moreover, our results suggest that thermochemically stable particles (e.g., ZrO2) with a high melting point and a low vapor pressure exhibited micro-scale diffusion behaviors, in contrast to millimeter-scale diffusion behaviors of common doping additives (e.g., ZnO), which are more suitable as a locally incorporated dopant for achieving location-specific property tuning. Test cases of selectively doped piezoelectric components in predefined patterns highlight the potential of the proposed approach in creating novel piezoelectric materials with programmable location-specific properties.

# 1. Introduction

The electromechanical coupling and conversion efficiency of polycrystalline piezoelectric ceramics are strongly affected by intrinsic microstructures in the materials [1,2]. Manipulating the microstructures alters the electromechanical interaction between the mechanical and electrical states in piezoelectric ceramics, resulting in tailorable piezoelectric behaviors. In traditional ceramic manufacturing, dopants have been widely used to tailor the grain structures and properties of piezoceramics by restricting the grain growth during sintering. Other traditional manufacturing techniques, such as tape casting and templating [3, 4], utilize directional particle alignment to achieve templated grain

growth control for better dielectric and piezoelectric properties. All these traditional techniques can only homogeneously vary the microstructures in a ceramic and are not capable of strategically controlling the microstructures at varying spatial locations. In recent years, additive manufacturing (AM) technologies have been adopted as an effective approach to regulate the macroscopic piezoelectric properties of piezoelectric materials [5], but much of the research is currently centered around design and manipulation of meso-scale architectural units (rather than grain-scale microstructures) to introduce location-specific electric displacement vectors, which have inherent limitations in achieving high functionality due to high structural porosity [6,7].

 $\hbox{\it E-mail address:} \ xuan-song@uiowa.edu \ (X.\ Song).$ 

<sup>\*</sup> Corresponding author.

<sup>&</sup>lt;sup>1</sup> Current address: School of Electromechanical Engineering, Guangdong University of Technology, Guangzhou, Guangdong 510006, China.

<sup>&</sup>lt;sup>2</sup> Current address: Foshan Nanhai Guangdong University of Technology CNC Equipment Cooperative Innovation Institute, Foshan, Guangdong 528225, China.

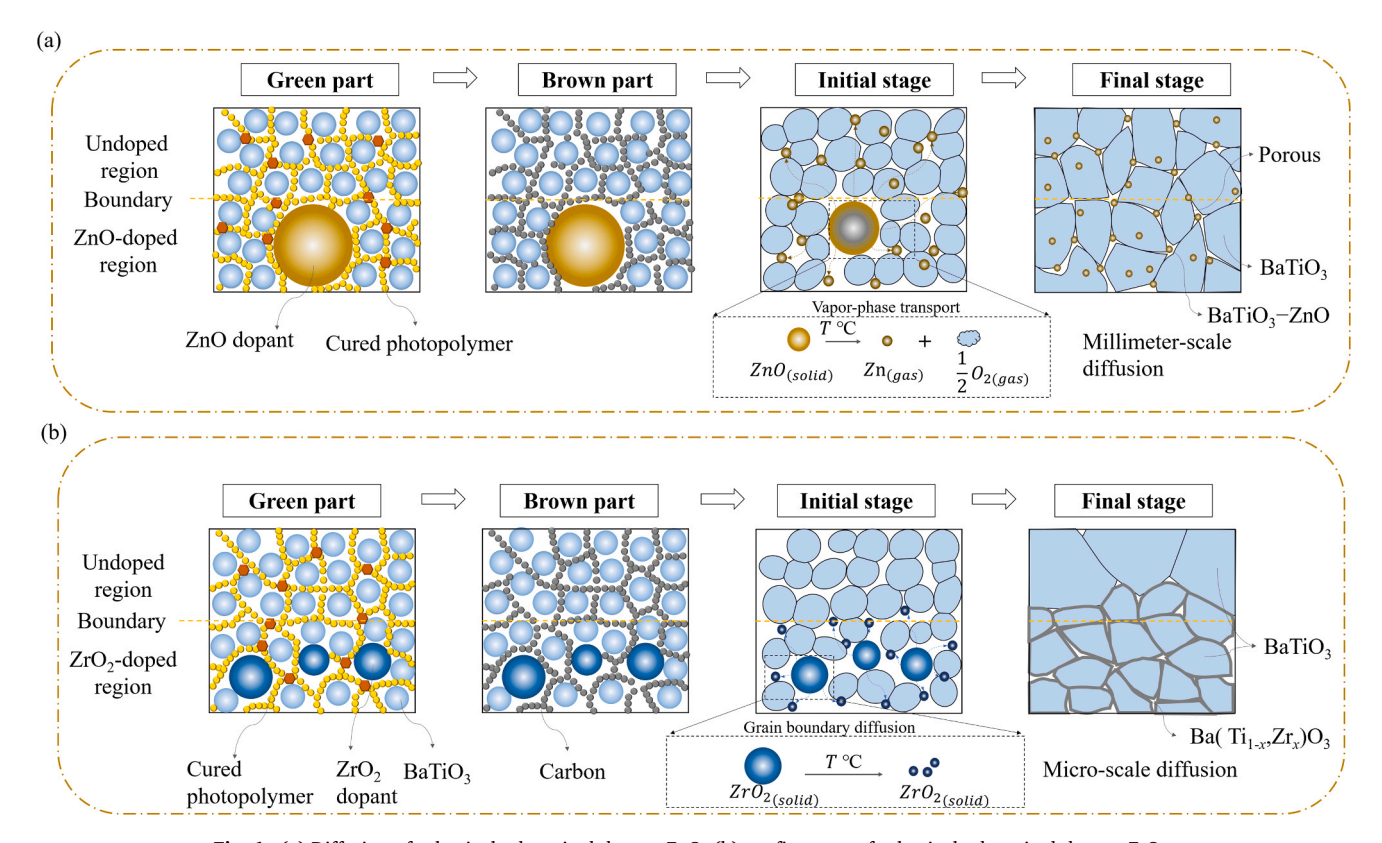


Fig. 1. (a) Diffusion of selectively deposited dopant ZnO; (b) confinement of selectively deposited dopant ZrO2.

Here we report an AM fabrication strategy to spatially tune the microstructures of piezoelectric ceramics at the grain scale for programmable piezoelectric performance. This is achieved through selectively incorporating dopants into the ceramic materials via a multi-material ceramic AM process [8,9]. A key challenge in achieving selective doping of ceramics lies in the confinement of a locally deposited doping additive in predefined locations without diffusing into un-specified regions. Common doping additives, such as ZnO [10], usually exhibit millimeter-scale diffusion behaviors as a result of vapor-phase diffusion in a highly porous debinded part under elevated temperatures, which give rise to unintentional inhibition in the undoped regions of selectively doped specimens, as shown in Fig. 1a. In order to achieve location-specific inhibition effect, we utilize thermochemically stable particles as doping additives, e.g., ZrO2 [11,12], with suppressed vapor-phase diffusion and limited grain boundary diffusion, as shown in Fig. 1b. The high melting point and low vapor pressure of ZrO<sub>2</sub> restrict its diffusion distance to be as low as 10 µm, in contrast to a diffusion range of more than 500 µm by common doping additives, such as ZnO.

In this study, the influence of ceramic solids loading in feedstock materials on the grain structures and properties [13–15] of printed parts is first investigated. Different doping materials, i.e., ZnO and ZrO<sub>2</sub>, with varying concentrations (0–2 wt%) were added in the feedstocks to induce grain growth inhibition and property tuning [16,17]. Different selectively doped specimens were created and characterized to demonstrate the localized microstructure control behaviors of dopants. The mechanism of dopant redistribution is discussed and verified with numerical modeling. Finally, three-dimensional (3D) structures containing location-specific dopants are demonstrated to highlight the feasibility of selective doping in tuning properties of piezoelectric ceramics.

## 2. Experimental section

# 2.1. Feedstock preparation

Barium titanate (BTO, < 2 µm, Sigma-Aldrich, Darmstadt, Germany) was used as a model material. Zinc oxide (ZnO, 74 µm, Alfa Aesar, Tewksbury, USA) and zirconium (IV) oxide (ZrO2, 5 μm, Sigma-Aldrich, Darmstadt, Germany) were selected as doping additives. BTO slurries were prepared by mixing as-received BTO powders with a mixture of photocurable resins, which is comprised of two commercial resins in a 1:1 weight ratio for suitable photosensitivity and accuracy, including a Formlabs resin (FLGPCL01, Formlabs, Boston, USA) and an Anycubic resin (white, ANYCUBIC, Shenzhen, China). Dianycubicspersant (phosphate ester, PS-131, AkzoNobel, Amsterdam, Netherlands) was added as a dispersant with an optimized concentration of 0.8 wt% (on a weight basis of the dry powder) to stabilize the particle distribution. Doped slurries were prepared by mixing the BTO slurries with a dopant at different weight ratios from 0.5 wt% to 2 wt%. Concentrations higher than 2 wt% were not tested since our experiments indicate the concentration of 2 wt% achieved the smallest possible grain size close to the original particle size. All slurries were first manually stirred for 2 min and then fully mixed in a ball mill machine for 2 h at a speed of 300 RPM. Finally, the slurries were degassed three times (10 min each) in a vacuum of -1.5 bar.

#### 2.2. Sample fabrication

To investigate the dopant-ceramic interaction and its effect on the microstructures, five groups of specimens were printed with different combinations of slurries, as summarized in Table S1. To investigate the effect of green density on the microstructures, group #1 specimens were prepared with pure BTO slurries with ceramic solids loading of 70 wt%, 80 wt%, and 85 wt%, respectively. To study the role of ZnO in the grain growth control, group #2 specimens were printed with a 0.5 wt% ZnO-

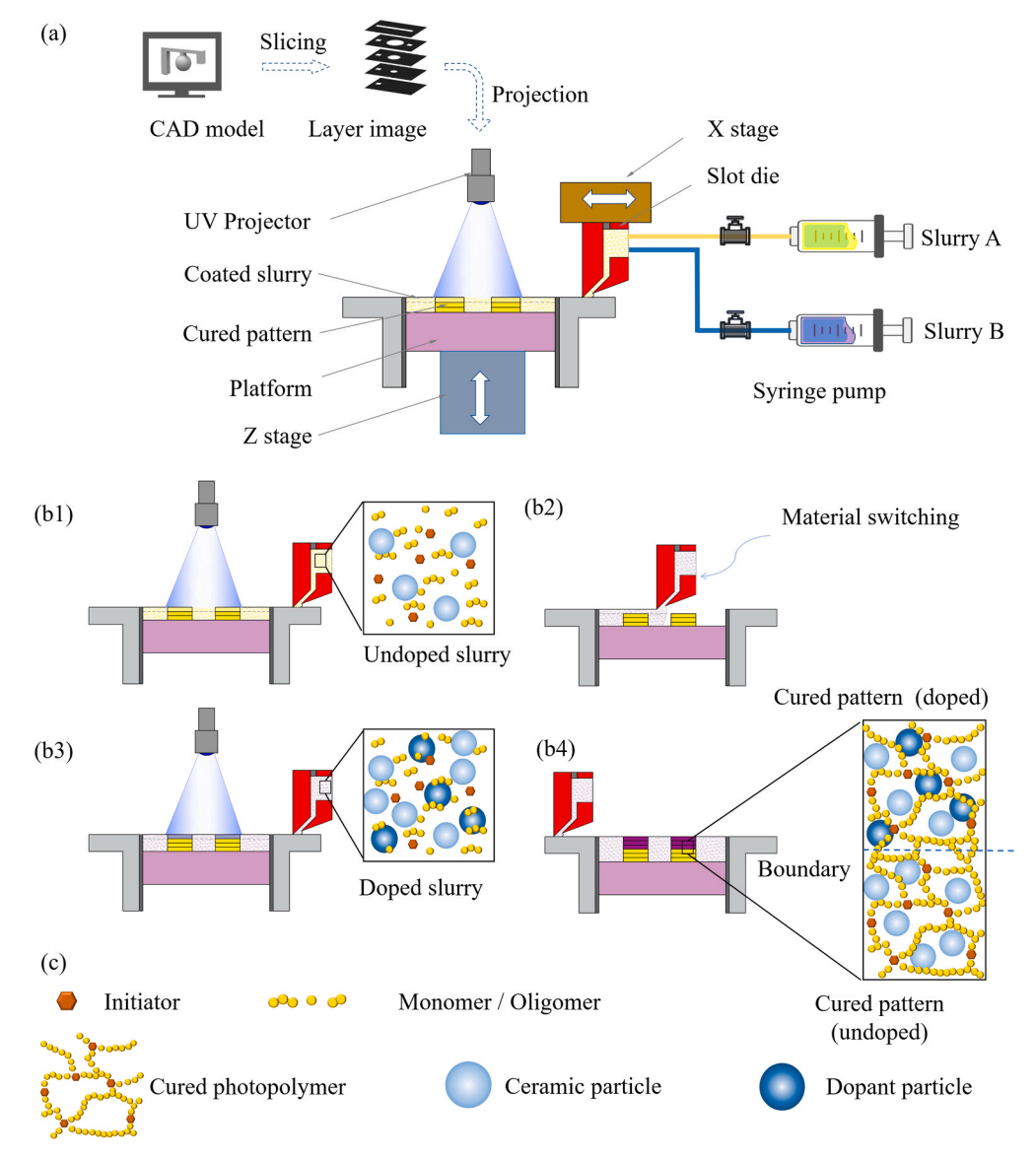


Fig. 2. (a) A schematic of the SEPS process with material switching. (b) The printing process of SEPS. (c) Different material ingredients.

doped and a 2 wt% ZnO-doped slurry. To study the role of ZrO<sub>2</sub> in the grain growth control, group #3 specimens were printed with a 1 wt% and a 2 wt% ZrO<sub>2</sub>-doped slurry, respectively. The solids loadings of all the doped slurries were maintained at 80 wt%, comprising both BTO particles and dopant particles. To demonstrate localized microstructure control, selectively doped specimens (group #4) were fabricated, half of which was printed with a 2 wt% ZnO-doped slurry or a 2 wt% ZrO<sub>2</sub>-doped slurry ( $\sim$  1 mm), and the other half with an 80 wt% undoped slurry ( $\sim$  1 mm). All the test samples from group #1 to #4 were printed in a block shape with a dimension of  $8\times8\times2$  mm (length -  $\times$  width  $\times$  height) and a layer thickness of 75 µm. To demonstrate the localized doping in 3D structures, samples were selectively doped in half of their volumes; the doped and undoped regions were separated by a plane with different angles, i.e.,  $0^{\circ}$ ,  $45^{\circ}$ , and  $90^{\circ}$ .

### 2.3. Post-processing

De-binding and sintering processes were implemented to remove the photopolymer resin in the green parts and densify the compacts into dense ceramic parts. In the de-binding step, green parts were fired at a temperature of  $600\,^{\circ}\text{C}$  for  $180\,\text{min}$  in an argon atmosphere in a tube furnace (STF150, Carbolite-Gero LLC, Hope Valley, UK). In this step, the

photopolymer in the green part was decomposed, and residue char was left over to bind BTO particles and/or dopant particles together. The resulting part then underwent a high temperature sintering process at 1330  $^{\circ}$ C with a soaking time of 240 min in a regular muffle furnace (HTF18, Carbolite-Gero LLC, Hope Valley, UK). Finally, the resulting specimens were polished and coated with platinum electrodes, as described in Fig. S1 and Table S2. After that, a corona poling process was conducted to induce piezoelectric properties in the specimens. Detailed experimental methods and parameters are discussed in the Supporting Material.

# 2.4. Microstructure characterization

The microstructures of the fabricated samples were characterized through scanning electron microscopy (SEM) to establish their dependence on process parameters (i.e., green density, dopant, and dopant distribution). For each sample, the cross-section perpendicular to the printing direction was polished by procedures listed in Table S2. Then the sample was thermally etched to reveal the well-developed microstructures, including individual grains, different phases, grain boundaries, and porosity. The thermal etching was carried out under a temperature of 1200 °C for a soaking time of 120 min in a muffle

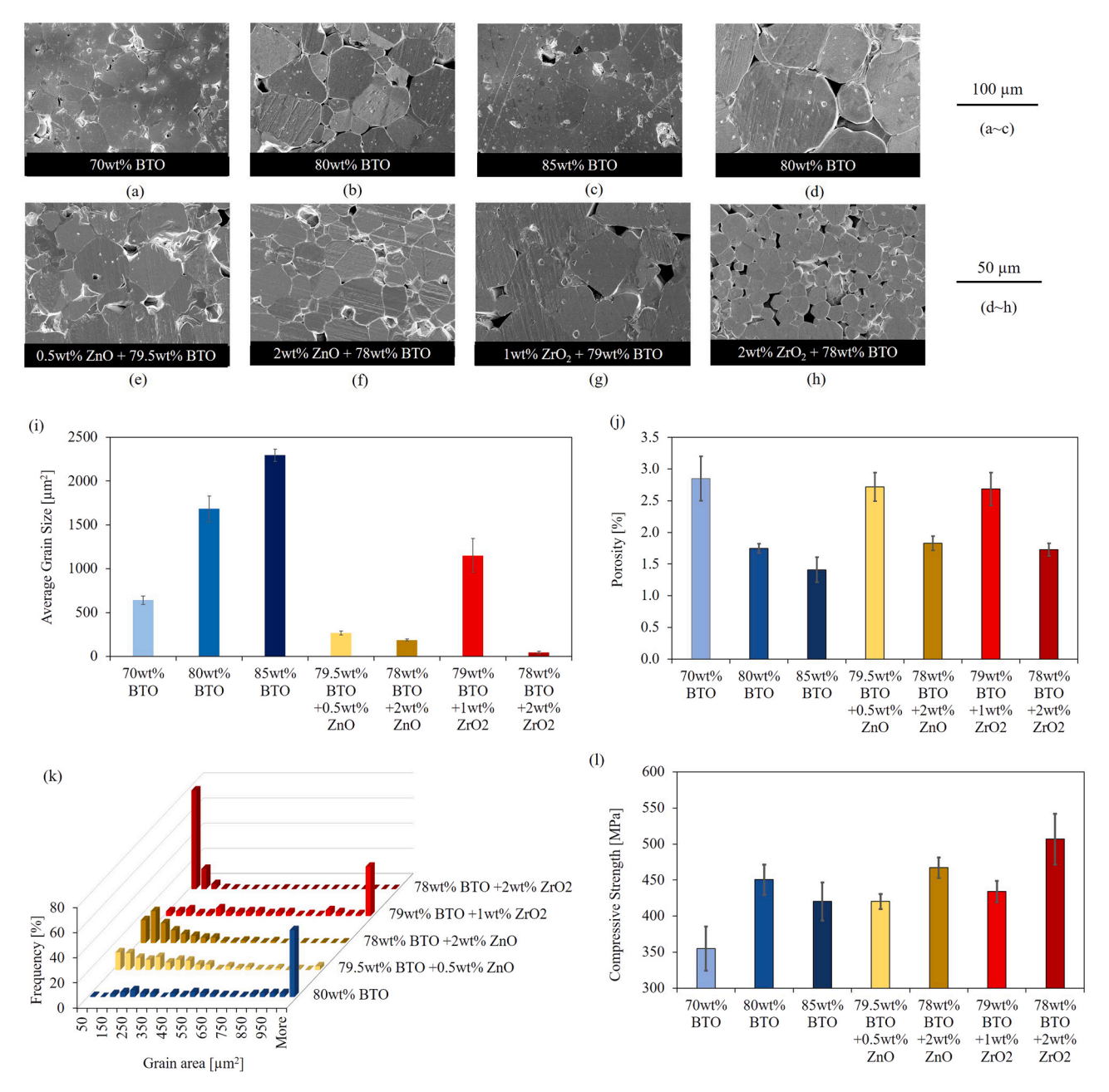


Fig. 3. Effects of doping on the microstructures and compressive strength of the printed BTO parts: SEM images at 500X magnification for the undoped BTO samples with solids loading of: (a) 70 wt%, (b) 80 wt%, (c) 85 wt%. SEM images at 1000X magnification for the 80 wt% BTO samples doped with (d) 0%, (e) 0.5 wt% ZnO, (f) 2 wt% ZnO, (g) 1 wt% ZrO<sub>2</sub>, and (h) 2 wt% ZrO<sub>2</sub>. The solids loadings of the samples were labeled in the SEM images for comparison. (i) The Average grain size. (j) Average porosity. (k) Grain area distribution. (l) Compressive strength.

furnace. The prepared surface was finally sputter-coated with a thin layer of platinum (around 10 nm) for better electron conductivity prior to SEM imaging. The microstructures were quantified through measurements of the porosity, grain size, grain distribution, and other geometry information (maximum diameter, solidity, and circularity) using ImageJ [18] as described in Fig. S2. Metrics including grain area, maximum diameter, circularity, and solidity were calculated based on the SEM images to characterize the microstructures in a given specimen. Energy dispersive X-ray spectroscopy (EDS/EDX) was used to detect the distribution of Zn or Zr element in sintered specimens with selectively doped patterns. X-ray diffraction (XRD) was used to identify the crystalline structures of sintered specimens.

### 2.5. Property characterization

The piezoelectric charge constant  $d_{33}$  of the specimens was measured using a piezoelectric charge constant meter (PKD3-2000, PolyK Technologies LLC, Philipsburg, USA) at a force-frequency of 110 Hz. The piezoelectric voltage constant  $g_{33}$  was calculated via the equation  $g_{33}=d_{33}/\varepsilon_r\varepsilon_\theta$ . The dielectric permittivity was calculated via  $\varepsilon_{33}=\varepsilon_r\varepsilon_\theta$ , where  $\varepsilon_\theta=8.854\times 10^{-12}\mathrm{F}$   $m^{-1}$  is the permittivity of air,  $\varepsilon_r$  is the relative permittivity of a measured material. The  $\varepsilon_r$  and  $\tan\theta$  were measured using an LCR meter (TG2811D, TONGHUI, Changzhou China) at 1 kHz frequency, signal source output resistance  $100~\Omega$ , a signal level of  $1.0~\mathrm{V}$ , and a parallel equivalent circuit. The compressive strength of the specimens was measured with a tensile tester (TestResqurces,  $1000~\mathrm{lbf}$  Actuator, Shakopee, USA) at a load rate  $0.5~\mathrm{mm/min}$  and a maximum

force 4200 N. These properties were selected to demonstrate the tunability of selective doping over the macroscopic performance of piezoelectric ceramics, and the generated knowledge can be easily extended to other important properties of the materials, such as strength, hardness, and electromechanical coupling coefficient.

#### 3. Results and discussion

#### 3.1. Fabrication process

Additive manufacturing of ceramics is increasingly gaining importance in many industry areas [19–22], thanks to its flexibility in achieving complex ceramic structures that are extremely difficult to produce with traditional machining methods due to the brittleness of ceramics. Among different AM technologies for ceramic fabrication, ceramic stereolithography (CSL) has been one of the most effective methods to create high precision and fully dense ceramics [13,16,17, 23]. In this study, we used a CSL-based AM process, named suspension-enclosing projection stereolithography (SEPS), to achieve dopant-controlled printing of piezoelectric ceramics. Compared to other ceramic AM technologies, the SEPS process can achieve multi-material printing of low-photosensitivity ceramic slurries utilizing a shear-controlled material feeding and layer recoating technique [8,9].

A schematic of the SEPS process is presented in Fig. 2a. The fabrication system mainly consists of a customized light engine, a shearcontrolled layer recoater, and a cooling building platform. On fabrication initialization, the layer recoater delivered a uniform thin layer of a ceramic slurry onto the cooling building platform with a carefully controlled shear force. The deposited slurry on the cooling platform was immediately cooled down by a chilling semiconductor plate mounted under the building platform, which can increase the yield strength by ten times. After that, the light engine projected a digital image with a wavelength of 405 nm via a digital micromirror device (DMD) (Texas Instruments) onto the surface of the fresh layer. To enable selective doping during the SEPS process, the feedstock material was dynamically switched between multiple ceramic slurries containing dopants at different concentrations (0-2 wt%) and was selectively cured in a predefined 3D architecture, as illustrated in Fig. 2b and c. For example, after the printing with a slurry A was finished, a slurry B was extruded into the layer recoater to flush out the slurry A; following that, the printing with the slurry B was initialized. It should be noted that, the material switching method used in our present work can only change the dopant concentration across different layers but not within the same layer. This can be further improved through involving a multi-recoater deposition system and a slurry cleaning module, similar to the material switching approach used in prior work [24,25]. Five groups of samples were fabricated with different doping parameters. Samples in test group #1-3 were fabricated with a single material, and those in test group #4 and #5 were fabricated with two slurries containing different dopant concentrations. The printed specimens via the SEPS process contain piezoelectric ceramic particles (i.e., BTO) and doping additives embedded in a solid resin matrix (i.e., green parts), which were further debinded and sintered to attain pure ceramic components [7].

## 3.2. Effects of doping on microstructures and mechanical properties

We first investigated the effects of different doping parameters (ceramic solid loading, dopant type, and dopant concentration) on the microstructures and compressive strength of BTO components printed with homogenous doping additives. Fig. 3a–c indicate that the grain size increased as the solids loading of ceramics in green parts increased from 70 wt% to 85 wt%. Fig. 3e–h show that the grain size decreased as the amount of ZnO addition increased from 0.5 wt% to 2 wt%, or the amount of ZrO<sub>2</sub> addition increased from 1 wt% to 2 wt%. It should be noted that in our experiments, we tested different concentrations for both dopants from 0 to 2 wt%. However, the rates of change in the grain

structures (e.g., grain size) achieved by the two doping materials were different as the dopant concentration increased. For example, for ZnO, a concentration of 0.5 wt% began to inhibit the grain growth, while the concentrations of 1 wt% and 2 wt% did not make too much difference in the grain structures. In contrast, doping with ZrO $_2$  did not induce sufficient grain growth inhibition until the dopant concentration increased to 1 wt%. Therefore, different concentrations were selected for ZnO (0.5 wt% and 2 wt%) and ZrO $_2$  (1 wt% and 2 wt%) to demonstrate their typical grain microstructures.

Quantitative metrics of the fabricated microstructures, including average grain size, porosity, grain area, are presented in Fig. 3i-k. Other microstructure metrics such as circularity and solidity are shown in Figs. S3 and S4. As can be seen in Fig. 3i, as the solids loading of BTO increased from 70 wt% to 85 wt%, the average grain size increased from  $\sim$ 640  $\mu$ m<sup>2</sup> to  $\sim$ 2300  $\mu$ m<sup>2</sup>. After a dopant (i.e., ZnO or ZrO<sub>2</sub>) was added, the grain growth was inhibited tremendously and was influenced by the dopant type and concentration. Doping ZnO with a concentration of 0.5 wt%, for example, inhibited the grain to an area of  $\sim$ 266  $\mu$ m<sup>2</sup>, which is only one-ninth of the grain area of the 80 wt% undoped BTO sample; increasing the dopant concentration to 2 wt% or higher reduced the grain area slightly to 200 µm<sup>2</sup> with a more concentrated distribution (Fig. 3k). In comparison to ZnO that led to relatively stable grain growth inhibition effect at different concentrations, ZrO2 exhibited relatively poor grain growth inhibition at a low concentration (i.e., 32% grain size reduction at 1 wt% ZrO2 addition), but a stronger inhibition at a doping concentration of 2 wt% or higher (i.e., 98% grain size reduction). This difference between ZnO and ZrO2 in grain growth inhibition can be explained by their difference in grain boundary diffusion and vaporphase diffusion, which is discussed in detail in Section 3.3. Fig. 3i shows the influence of doping on the porosity of the fabricated BTO specimens. With a higher solids loading of ceramics in green bodies, the porosity reached as low as 1.4% with a relatively uniform grain size around 2300 μm<sup>2</sup>. Incorporating a dopant at a relatively low concentration (e.g., 0.5 wt%) increased the porosity from 1.8% to 2.7%, due to abnormal grain growth with grain size varying from 50 µm<sup>2</sup> to over 1000 μm<sup>2</sup>. Increasing the dopant to 2 wt% promoted the homogeneity of grain growth inhibition and consequently resulted in a homogeneous grain size distribution with a low porosity comparable to the undoped 80 wt% BTO sample.

Fig. 3l shows the effect of different doping parameters on the compressive strength of BTO specimens. The compressive strength of the undoped BTO samples reached its peak as the solids loading of the green part increased from 70 wt% to 80 wt% due to a much lower porosity. When the solids loading of the green part was further increased to 85 wt %, the compressive strength decreased as a result of a bigger grain size but a minor porosity improvement. A small amount of dopants, such as 0.5 wt% ZnO or 1 wt% ZrO2, led to a decrease in the compressive strength due to the heterogeneous grain size distribution and higher porosity, while a sufficient amount of dopants (2 wt% ZnO or 2 wt% ZrO2) evidently improve the compressive strength due to a homogeneous grain size distribution. Specifically, according to Fig. S4, the grain size was reduced by  $\sim\!40$  times while a 2 wt% of ZrO2 was added, and the grain area and diameter in the 2 wt% ZrO2 doped sample were distributed within a much narrower range.

# 3.3. Effects of doping on piezoelectric properties

An ideal piezoceramic is desired to exhibit a high magnitude of piezoelectric voltage constant  $g_{33}$ , high piezoelectric charge constant  $d_{33}$ , low dielectric permittivity  $\varepsilon_{33}$ , and dielectric loss (tan  $\delta$ ) [26]. A higher piezoelectric voltage constant and piezoelectric charge constant represent a higher electric field and better polarization that can be generated by the material per unit of mechanical stress applied or a greater mechanical strain experienced by a piezoelectric material per unit of electric displacement applied [27]. Lower loss indicates fewer limitations in the harvesting energy bandwidth [28]. Lower permittivity

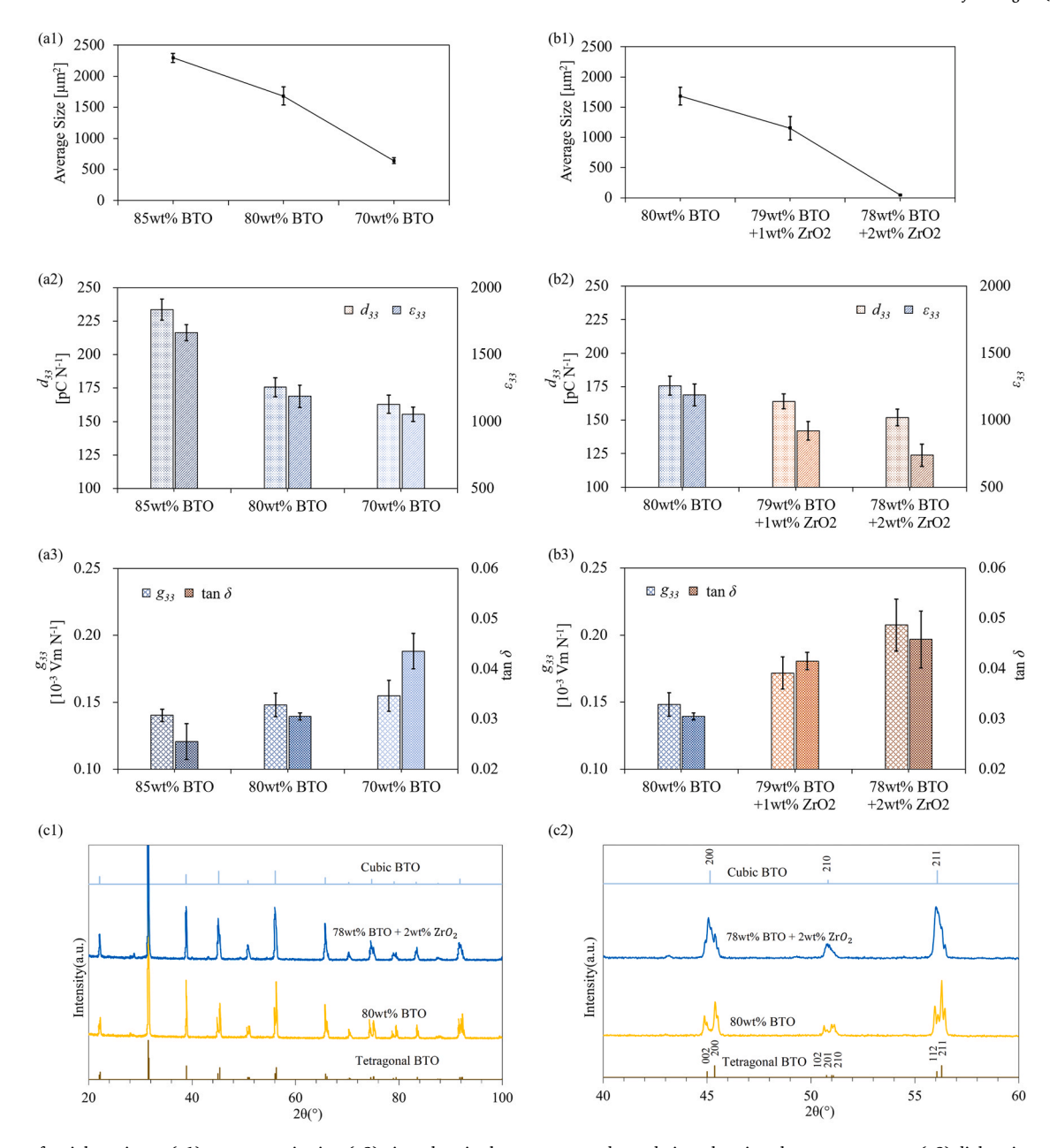


Fig. 4. Effects of weight ratio on: (a1) average grain size; (a2) piezoelectric charge constant  $d_{33}$  and piezoelectric voltage constant  $g_{33}$ ; (a3) dielectric permittivity  $\varepsilon_{33}$  and dielectric loss tan  $\delta$ . Effects of ZrO<sub>2</sub> concentration on: (b1) average grain size; (b2) piezoelectric charge constant  $d_{33}$  and piezoelectric voltage constant  $g_{33}$ ; (b3) dielectric permittivity  $\varepsilon_{33}$  and dielectric loss tan  $\delta$ . (c1) XRD patterns for 80 wt% BTO and 2 wt% ZrO<sub>2</sub> doped BTO. (c2) Zoom-in view of XRD patterns for all samples from  $40^{\circ}$  to  $60^{\circ}$ .

values are preferred for piezoelectric material in high frequency or power applications to minimize the electric power losses.

The measurement results of the piezoelectric properties of the BTO specimens fabricated under varying doping parameters are given in Fig. 4. The corresponding grain size is given in Fig. 4a1 and b1. For the undoped samples (Fig. 4a1–a3), as the solids loading and grain size increased, the piezoelectric charge constant  $d_{33}$  and dielectric permittivity  $\varepsilon_{33}$  increased, and the dielectric loss  $\tan\delta$  and piezoelectric voltage constant  $g_{33}$  decreased. For the doped samples (Fig. 4b1–b3), doping with 2 wt% ZrO<sub>2</sub> resulted in an unfavorable 9% drop in the piezoelectric charge constant  $d_{33}$  and a decrease of 38% in the dielectric permittivity  $\varepsilon_{33}$ . On the other hand, it also contributed to a 48% increase in the dielectric loss and an increase of 49% in the piezoelectric voltage constant  $g_{33}$ .

The XRD patterns of 80 wt% BTO and 2 wt% ZrO<sub>2</sub> doped BTO are shown in Fig. 4c1. A tetragonal BTO phase and a cubic BTO phase are

given in the figure as references. The zoom-in view of the XRD patterns in the range from 40° to 60° (Fig. 4c2) indicates a clear splitting phenomenon of the diffraction peaks at (002,200), (102,201,210), and (112,211), which are used as the identification of a tetragonal phase structure in the sintered ferroelectric BTO [12,29,30]. However, symmetric single peaks without splitting were observed in the XRD pattern of ZrO<sub>2</sub>-doped BTO sample, which is close to the cubic phase structure of BTO powder without sintering. This result suggests that the dopant ZrO<sub>2</sub> inhibits the formation of a tetragonal phase structure. Since a tetragonal phase contributes to a high piezoelectric charge constant d<sub>33</sub> [31], the ZrO<sub>2</sub>-doped sample exhibited a lower piezoelectric charge constant d<sub>33</sub> as the doping concentration increased.

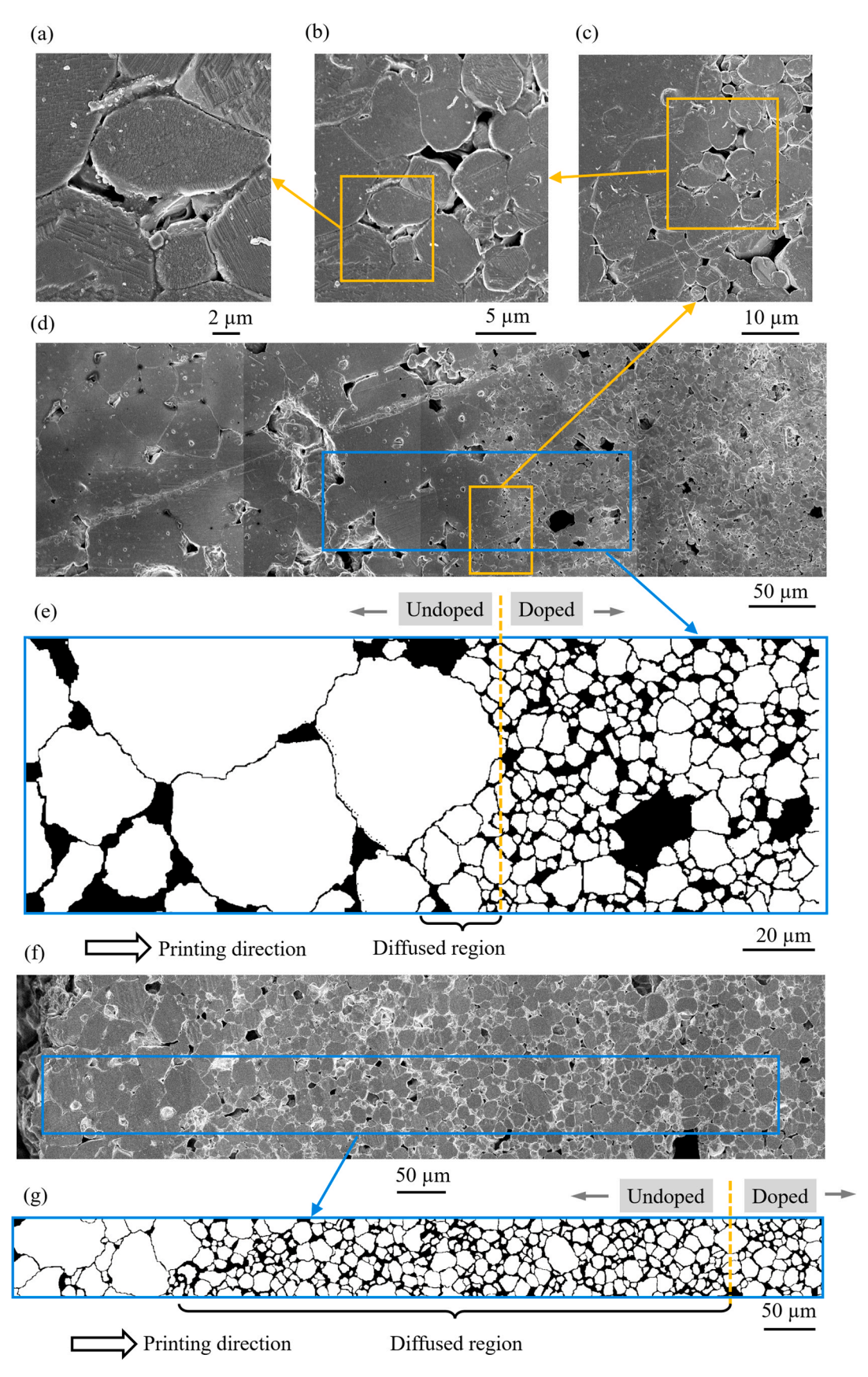


**Fig. 5.** The microstructures in the diffused regions: (a) 10,000X magnification; (b) 4000X magnification; (c) 2000X magnification; (d) the cross-section of a ZrO<sub>2</sub>-doped sample; (e) processed grain structures around the diffused region; (f) the cross-section of a ZnO-doped sample; (g) processed grain structures around the diffused region. (For interpretation of the references to color in this figure legend, the reader is referred to the web version of this article.)

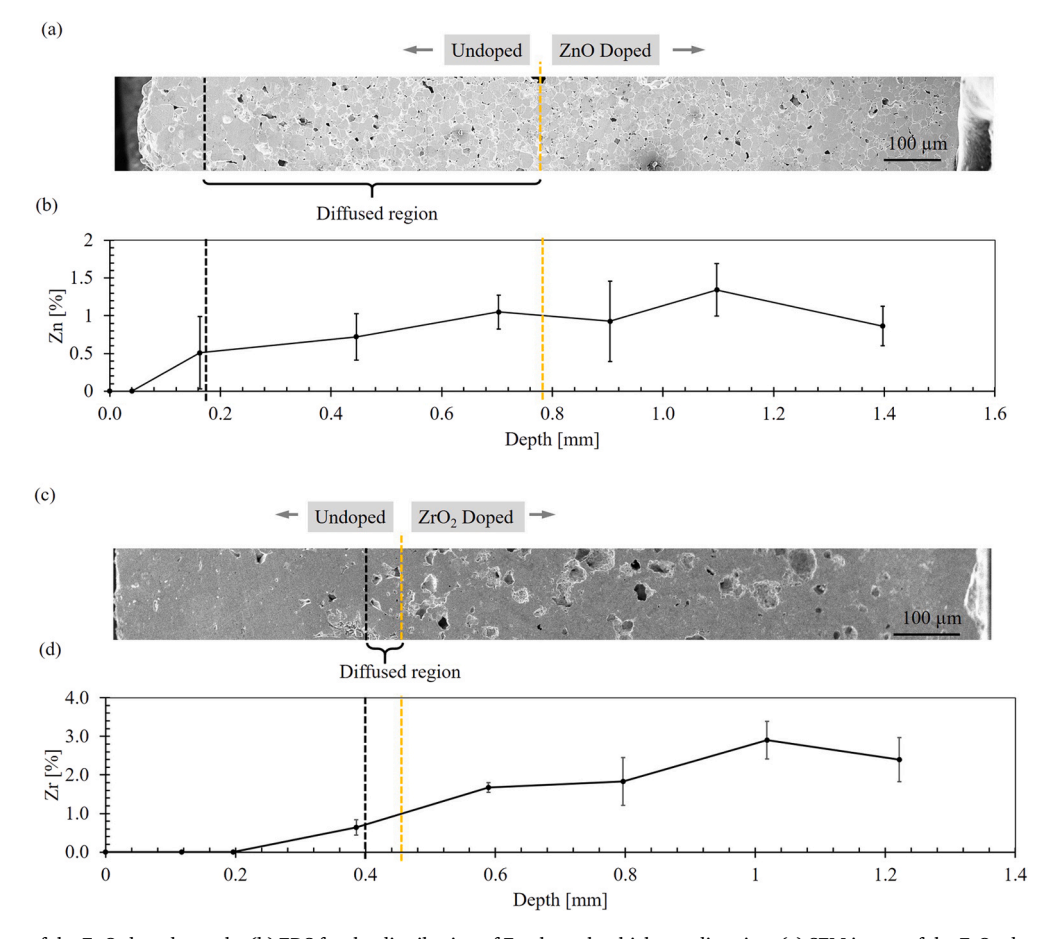


Fig. 6. (a) SEM image of the ZnO-doped sample. (b) EDS for the distribution of Zn along the thickness direction. (c) SEM image of the  $ZrO_2$ -doped sample. (d) EDS for the distribution of Zr along the thickness direction. (For interpretation of the references to color in this figure legend, the reader is referred to the web version of this article.)

#### 3.4. Localized microstructure control

#### 3.4.1. Characteristics of dopant diffusion

Fig. 5a–d shows the diffusion characteristics of different doping additives in selectively doped BTO samples. Half of each sample was doped with ZnO or ZrO<sub>2</sub> at a concentration of 2 wt%. The grain structures are shown in Fig. 5e and g, where the yellow dash lines represent the designed material boundary between the doped and undoped regions prior to sintering. A diffused region was identified between the designed material boundary and the actual boundary. The distance of the diffused region for ZrO<sub>2</sub> was measured as 10–60  $\mu$ m (refer to Fig. 5e), which is less than the layer thickness used in the printing (~75  $\mu$ m), indicating a precise localized control of grain sizes using ZrO<sub>2</sub> as a doping agent. In contrast, the diffusion distance in the ZnO-doped sample (Fig. 5g) was measured as more than 500  $\mu$ m, suggesting a higher redistribution behavior of the dopant during sintering.

The EDS maps of doping elements (i.e., Zn or Zr) along the thickness direction (horizontal) of the selectively doped samples are shown in Fig. 6. The SEM images of the ZnO-doped sample and the ZrO<sub>2</sub>-doped sample are shown in Fig. 6a and c, respectively, where the left side of the designed material boundary (yellow dash line) is the undoped region, and the right side is the doped one. The EDS result in Fig. 6b shows that Zn element increased from 0% to 1.05% as the depth increased from 0 to 0.7 mm. The region between x=0.16 mm and x=0.78 mm contained a high concentration of Zn around 1%, which led to undesired grain inhibition beyond the designed material boundary. The EDS result for Zr element in Fig. 6d shows that Zr element decreased to 0.64% at the

diffusion boundary located at x=0.39 mm, leaving a narrower diffused region beyond the designed material boundary (i.e., between x=0.39 mm and x=0.45 mm).

# 3.4.2. Mechanism of dopant redistribution

In selectively doped BTO samples, each dopant particle was surrounded by more than thousands of BTO particles. Despite such a low dopant concentration, some area in the undoped region still underwent grain growth inhibition. We believe this was caused by the redistribution behavior of dopant particles during the sintering.

The ZnO redistribution was likely dominated by vapor-phase diffusion, since no liquid phase exists in the BTO–ZnO matrix below 1350 °C and ZnO possesses a high vapor pressure (e.g.,  $10^{-4}$  Torr at  $\sim\!1800$  °C) [32]. Refs. [32,33] reveal that ZnO remains at the grain boundaries of ZnO-doped samples below 1275 °C; as the temperature rises above 1275 °C, Zn²+ cations are generated from the vapor-phase diffusion defined in Eq. (1) and enter the lattice of BTO [32]. The incorporation of Zn²+ cations into the BaTiO₃ lattice takes place at Ba²+ sites as an isovalent dopant [32,33]. Therefore, in the sintering of BTO specimens at a high temperature of 1330 °C (4 h soaking time), Zn²+ can rapidly diffuse beyond the doped region and enter a wider area in the undoped region.

$$ZnO_{(solid)} \stackrel{\iota \sim C}{\Leftrightarrow} Zn_{(gas)} + \frac{1}{2}O_{2} \quad _{(gas)}$$
 (1)

On the contrary, doping with  $ZrO_2$  generated a much clearer boundary between the doped and undoped regions with a narrow diffused area. This controlled diffusion is governed by the grain

boundary diffusion, because of the high melting point (2700 °C) and low vapor pressure (10 $^{-4}$  Torr at  $\sim\!2200$  °C) of  $ZrO_2$  compared to those of ZnO. According to Refs. [11,12],  $ZrO_2$  particles exist at the grain boundaries of BTO at temperatures lower than 1320 °C. When sintered above 1320 °C as in our work,  $Zr^{4+}$  cations diffuse into the outer shell of BTO grains, forming a core-shell grain structure. The incorporation of  $Zr^{4+}$  into the surrounding BTO crystals hinders the further diffusion of  $Zr^{4+}$  in the lattice, resulting in a well-controlled grain growth inhibition.

Considering the fact that the two dopants used in our study have different particle sizes (ZnO  $\sim\!74~\mu m$  and ZrO $_2\sim\!5~\mu m$ ), the discussion would not be complete without a few words about the potential effect of the particle size on the diffusion. From a thermodynamic point of view, the rate of diffusion is expected to decrease with increase in particle size, since the surface area of smaller particles is much higher than that of larger particles at the same concentration, thus requiring lower driving energy for diffusion. Contrary to this expectation, our experiment results indicate that ZrO $_2$  (smaller particle size) led to a much shorter diffusion distance (5  $\mu$ m) than ZnO under the same sintering condition. Therefore, we believe the particle size did not play a significant effect on the diffusion of the dopants during the sintering in our process.

In summary, ZnO exhibits millimeter-scale diffusion behaviors as a result of vapor-phase diffusion in a highly porous BTO lattice, which gives rise to undesired inhibition in undoped regions of selectively doped specimens. In comparison, ZrO<sub>2</sub> with suppressed vapor-phase diffusion and core-shell grain formation only diffuses a micro-scale distance in the material and is considered as a more suitable dopant for achieving localized grain growth control. Future experimental studies are still needed to verify this hypothesized mechanism.

### 3.5. Numerical modeling of dopant redistribution behavior

A phase field model was adopted to describe the phase evolution and mass transfer processes in the dopant-ceramic interaction during sintering of SEPS-printed BTO parts. Two order parameters were employed to represent the microstructure of materials: (1) a conserved order parameter, or densify field  $\rho$ , describes the mass transfer that equals to 1 at the solid phase and 0 at vapor phase. The value of  $\rho$  varies smoothly but rapidly across boundary between solid and vapor; (2) a nonconserved order parameter, or phase variable  $\eta_{\alpha}$ , was used to distinguish different grain or particles in the solid phase. The subscript  $\alpha$  indicates  $\eta_{\alpha}=1$  in  $\alpha$ -th grain and 0 in other grains. The value of  $\eta_{\alpha}$  varies smoothly from 1 to 0 or from 0 to 1 at grain boundaries correspondingly. Finally, the total free energy of the system is given by a functional equation by two order parameters [34], as

$$F = \int_{r} \left\{ f(\rho, \{\eta_{\alpha}\}) + \frac{1}{2} \kappa_{\rho} |\nabla \rho|^{2} + \frac{1}{2} \kappa_{\eta} \sum_{\alpha} |\nabla \eta_{\alpha}|^{2} \right\} dr^{3}$$
 (2)

where  $\kappa_{\eta}$  and  $\kappa_{\rho}$  donate the gradient terms of the non-conserved order parameter  $\eta_a$  and the conserved order parameter  $\rho$ , respectively.  $f(\rho, \{\eta_a\})$  is the free energy density, expressed as

$$f(\rho, \{\eta_{\alpha}\}) = A[\rho^{2}(1-\rho)^{2}]$$

$$+ B\left[\rho^{2} + 6(1-\rho)\sum_{\alpha}\eta_{\alpha}^{2} - 4(2-\rho)\sum_{\alpha}\eta_{\alpha}^{2} + 3\left(\sum_{\alpha}\eta_{\alpha}^{2}\right)^{2}\right]$$
(3)

where A and B are constants. According to Refs. [35,36],  $\varepsilon_{\rho} = k_1 \left( 2\gamma_s - \gamma_{gb} \right) \delta$ ,  $\varepsilon_{\eta} = k_2 \gamma_{gb} \delta$ ,  $A = k_3 \left( 12\gamma_s - 7\gamma_{gb} \right)$  and  $B = k_4 \gamma_{gb} / \delta$  were obtained, where  $\gamma_s \approx 1 \text{ J/m}^2$  [37] is the surface energy and  $\gamma_{gb}$  is grain boundary energy (we assume  $\gamma_{gb} = 0.5\gamma_s$  due to insufficient data), respectively. The  $\delta$  is the grain boundary width, and  $k_1$ ,  $k_2$ ,  $k_3$ ,  $k_4$  are the constants used to normalize material parameters.

The evolution equations of density  $\rho$  is expressed in the Cahn-Hilliard equation:

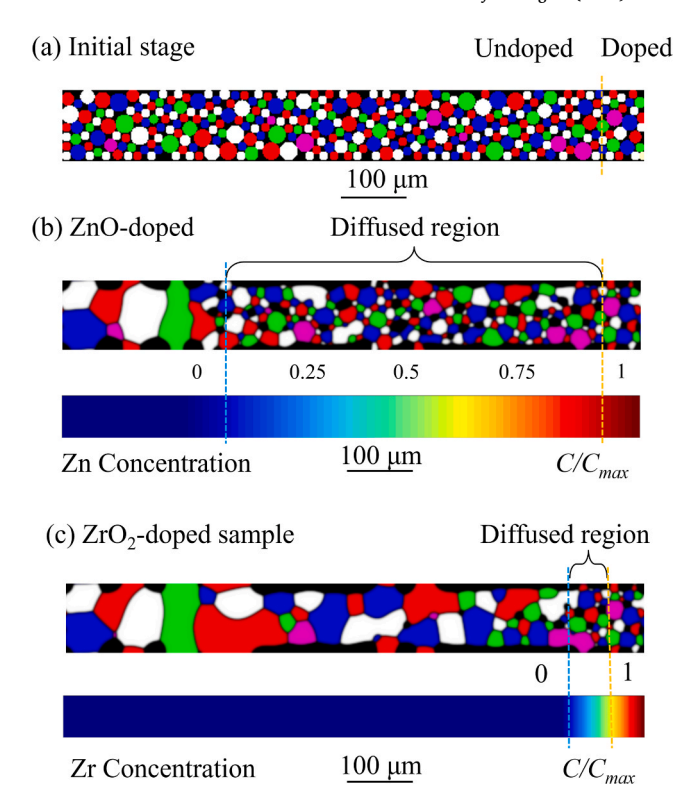


**Fig. 7.** (a) The initial stage of powder compact. (b) The diffused region in the final stage of sintering a ZnO-doped sample. (c) The diffused region in the final stage of sintering a ZrO<sub>2</sub>-doped sample. (For interpretation of the references to color in this figure legend, the reader is referred to the web version of this article.)

$$\dot{\rho}(r,t) = \nabla \cdot \left[ M \nabla \left( \frac{\partial f}{\partial \rho} \text{-} \kappa_{\rho} \nabla^2 \rho \right) \right] \tag{4}$$

where, the M is the modified diffusion mobility formulated by [38].

$$M = M_{vol}\phi(\rho) + M_{vap}[1 - \phi(\rho)] + M_{sf}\rho(1 - \rho) + M_{gb}\sum_{\alpha}\sum_{\alpha'\neq\alpha}(\eta_{\alpha}\eta_{\alpha'})$$
 (5)

where  $M_{vol}$ ,  $M_{vap}$ ,  $M_{sf}$  and  $M_{gb}$  represent the diffusion mobilities in the solid volume, vapor, along the surface and the grain boundary, respectively. Hence, following the work proposed by Ahmed et al. [35], the value of M is obtained via,  $M_i = D_i V_m/k_B T$ , where the suffix 'i' donates the different diffusion paths,  $D_i$  represents the corresponding diffusion coefficient, The  $V_m$  is the is the molar volume,  $k_B$  is the Boltzmann constant, and T is the sintering temperature. Here, since the data regarding surface and volume diffusion coefficients for BTO are insufficient, we adopted a calibration method similar to Ref. [37] to determine the values, i.e.,  $D_{vap} = D_0 exp(Q/kT)$ , where  $D_0$  ( $\approx 10^{-1}$ ) donates frequency factor for undoped BTO, and Q (= 3.18 eV) is the experimental activated energy of the vacancy diffusion [37]. The surface diffusion coefficient  $D_{sf}$  is set as 1000 times as the volume diffusion coefficient  $D_{vap}$ , and the diffusivity ratio ( $D_{sf}$ : $D_{gb}$ : $D_{vol}$ : $D_{vap}$ ) was set as 1000:100:10:1 to derive the other diffusion coefficients [38].

Similarly, the non-conserved grain evolution is in the form of the Allen-Cahn equation as  $\$ 

$$\dot{\eta}_{\alpha}(\mathbf{r},t) = -L \left( \frac{\partial f}{\partial \eta_{\alpha}} - \kappa_{\eta} \nabla^{2} \eta_{\alpha} \right) \tag{6}$$

where L, the grain boundary mobility coefficient characterizing grain boundary migration, was estimated following Ref. [39], as,  $L=4L_r/3\delta$ . We assume  $L_r$  is related to the concentration of dopant element Zn or Zr, as  $L_r=L_{r0}(1-C/C_{max})$ , in which  $C/C_{max}$  is the normalized

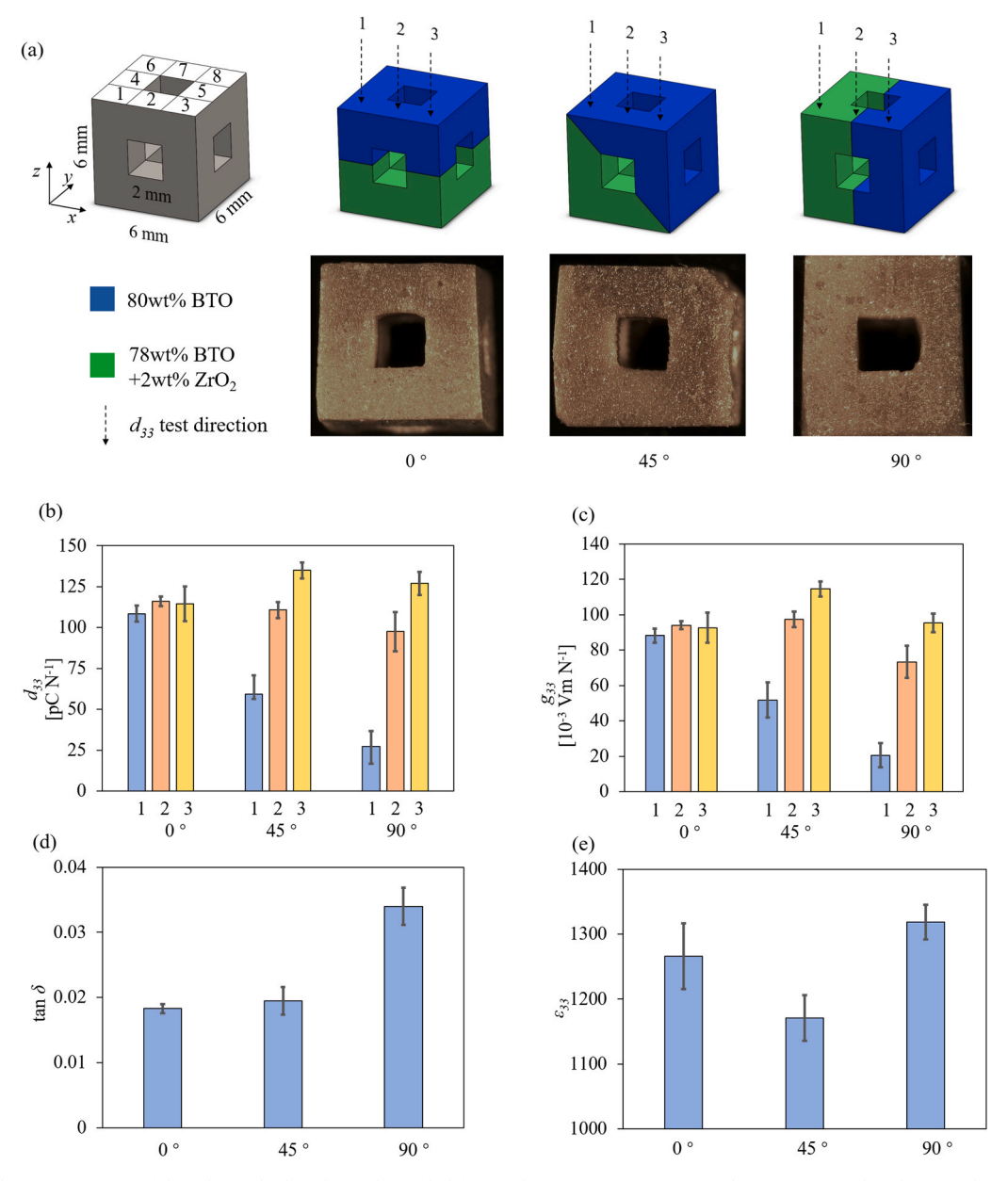


Fig. 8. The piezoelectric properties of the selectively doped samples with different doping patterns: (a) piezoelectric constant  $d_{33}$ ; (b) piezoelectric voltage constant  $g_{33}$ ; (c) dielectric permittivity  $\varepsilon_{33}$ ; (d) dielectric loss tan  $\delta$ .

concentration of Zn or Zr varying between 0 and 1; and  $L_{r0}$  is the grain boundary mobility estimated by the Arrhenius relation. Finally, the model was numerically implemented by using a finite difference method and an explicit time marching scheme. The dimensionless form is obtained by normalization with respect to reference time scale and length scale, which are 1  $\mu$ m and 1  $\mu$ s, respectively.

To further quantitatively elucidate the mechanism governing the diffusion of doped elements and its influence on the grain coalescence of BTO particle during sintering, comprehensive PFM simulations were conducted with results shown in Fig. 7. The simulation domain is set as 150  $\mu$ m x 700  $\mu$ m, and only grain coalescence among BTO particles were considered. The diffusion coefficients,  $D_i$ , were determined by the experimental calibration procedure using the data in Fig. 5. Five colors were used to mark different crystalline orientation among the particles. The powder compacts before sintering are shown in Fig. 7a. All particles were assumed in a spherical shape based on the experimental observation. The left side of the yellow dash line marks the doped region (~75  $\mu$ m), while the right side presents the undoped region. Fig. 7b and

c show the microstructures of sintered BTO particles doped by ZnO and ZrO<sub>2</sub>, respectively. The color bar shows the concentration gradient of Zn based on the experimental observation in previous sections. A normalized parameter,  $C/C_{max}$ , was applied to represent the concentration gradient, where C is the local concentration and  $C_{max}$  is the maximum concentration in the simulation domain. In the doped region, the high concentration of Zn or Zr undoubtedly inhibited the grain coalescence among BTO particles. However, in the ZnO-doped sample, Zn element underwent a significant diffusion into the undoped region that reduces the grain size of BTO in the diffused region. In comparison, the diffused region of Zr was much narrower than that of Zn (refer to Fig. 7c), resulting in a much greater average grain size than the ZnO-doped case. Both simulation results match the experimental observation discussed in Section 3.3.1. In addition, the effects of dopant concentration on the diffused region are presented in Figs. S5 and S6. With the dopant ZnO increasing from 0.25 wt% to 2 wt%, the diffused region extends in orders of magnitude. However, when dopant ZrO2 changes from 2 wt% to 3 wt%, the diffused region shows a negligible change.

#### 3.6. Test cases of 3D doping patterns

In this section, we demonstrate how different 3D doping patterns can alter the local properties of printed BTO components. The low diffusivity of  $\rm ZrO_2$  in sintered BTO offers the potential to accurately control location-specific properties of the material. That is, selectively doping a component in a predefined 3D architecture can spatially tune the microstructures of the components, which consequently enable programmable piezoelectricity.

Selectively doped BTO samples were fabricated in a hollow cubic shape as shown in Fig. 8a. The thickness of all the beams was designed as 2 mm to ensure uniform sintering. The samples were selectively doped in half of their volumes, and the doped and undoped regions were separated by a plane with three different angles, including  $0^{\circ}$ ,  $45^{\circ}$ , and  $90^{\circ}$ , as indicated in Fig. 8a. The doped half contained 78 wt% BTO and 2 wt% ZrO<sub>2</sub>, while the undoped half contained 80 wt% BTO. We divided the top face of each sample into 8 testing sub-regions to demonstrate the location-specific piezoelectric properties of different doping patterns. Considering the symmetry of the doping patterns, we selected the sub-regions (1, 2, 3) as the testing points to measure the piezoelectric properties.

Fig. 8b—e compare the piezoelectric properties for all the doping patterns (0°, 45°, and 90°). As can be seen in Fig. 8b and c, the 90° doping pattern demonstrated the greatest contrast in  $d_{33}$  and  $g_{33}$  measured from the three testing sub-regions, while the 0° doping pattern exhibited almost the same  $d_{33}$  and  $g_{33}$  in all the three sub-regions. This difference is attributed to distinct microstructural gradients in each sub-region in the three specimens stemming from varying doping patterns. For example, in the 0° doping pattern, the sub-regions 1 and 3 had the same microstructural gradient along the testing direction (i.e., the top half was comprised of large grains, and the bottom half of small grains), while in the 90° doping pattern, the sub-region 1 contained only small grains along the testing direction, and the sub-region 3 consisted of only large grains. Fig. 8d and e indicate different doping patterns led to different permittivity  $\varepsilon_{33}$  and dielectric loss tan  $\delta$ .

#### 4. Conclusion

In this paper, the effects of doping parameters (i.e., dopant type, dopant concentration, doping patterns, ceramic density) on the microstructures, thermodynamics of dopant diffusion, and final properties of 3D-printed piezoelectric ceramics were experimentally and numerically investigated. Two types of doping additives, ZnO and ZrO2, were studied and compared in terms of grain growth inhibition and redistribution properties. A concentration of 2 wt% for both dopants promoted the homogeneity of grain growth and consequently resulted in a higher compressive strength and lower porosity. A study of the microstructureproperty relationships indicates that a higher solids loading of BTO led to a relatively higher piezoelectric charge constant  $d_{33}$  and dielectric permittivity  $\varepsilon_{33}$  but produced lower dielectric loss tan  $\delta$  and similar piezoelectric voltage constant g<sub>33</sub>. By adding more dopants, the fabricated ceramics exhibited a worse piezoelectric charge constant  $d_{33}$ and dielectric loss but an improved dielectric permittivity  $\varepsilon_{33}$ piezoelectric voltage constant g<sub>33</sub>. Moreover, the experimental results on selective doping suggest that ZrO2 is more suitable as a locally incorporated dopant for achieving location-specific property tuning. Its high melting point and low vapor pressure limit its diffusion into the undoped region. With 2 wt% ZrO2 added in BTO, the XRD patterns indicate a clear inhibition of the splitting phenomenon of the diffraction peaks comparing to an undoped sample. The modification limits the lattice distortion by ionic displacement and leads to a lower piezoelectric charge constant  $d_{33}$ . Selectively doping a BTO component in a predefined pattern with ZrO2 can potentially create novel piezoelectric materials with programmable location-specific properties.

#### CRediT authorship contribution statement

Li He: Investigation, Validation, Data curation, Formal analysis, Writing – original draft. Xiao Wang: Writing – original draft, Software. Fan Fei: Data curation, Formal analysis. Lei Chen: Writing – review & editing, Supervision, Funding acquisition. Xuan Song: Conceptualization, Funding acquisition, Project administration, Supervision, Writing – review & editing

## **Declaration of Competing Interest**

The authors declare the following financial interests/personal relationships which may be considered as potential competing interests: Xuan Song reports financial support was provided by National Science Foundation. Lei Chen reports financial support was provided by National Science Foundation.

## Acknowledgement

He, L., Fei, F., and Song, X. acknowledge the support from the US National Science Foundation (NSF- CMMI-1825962). Chen, L. acknowledge the support from the US National Science Foundation (NSF- CMMI-2020527).

## Appendix A. Supporting information

Supplementary data associated with this article can be found in the online version at doi:10.1016/j.addma.2021.102407.

#### References

- S. Sturm, B. Jančar, Microstructure characterization of advanced ceramics. Advanced Ceramics for Dentistry, Elsevier, 2014, pp. 151–172, https://doi.org/ 10.1016/b978.0.13-394619-5.00008.0
- [2] R.L. Coble, Diffusion models for hot pressing with surface energy and pressure effects as driving forces, J. Appl. Phys. 41 (12) (1970) 4798–4807, https://doi.org/ 10.1063/1.1658543.
- [3] Y. Kan, P. Wang, Y. Li, Y.-B. Cheng, D. Yan, Fabrication of textured bismuth titanate by templated grain growth using aqueous tape casting, J. Eur. Ceram. Soc. 23 (12) (2003) 2163–2169, https://doi.org/10.1016/S0955-2219(03)00035-9.
- [4] S.H. Hong, S. Trolier-McKinstry, G.L. Messing, Dielectric and electromechanical properties of textured niobium-doped bismuth titanate ceramics, J. Am. Ceram. Soc. 83 (1) (2000) 113–118, https://doi.org/10.1111/j.1151-2916.2000.tb01157.x.
- [5] C. Chen, X. Wang, Y. Wang, D. Yang, F. Yao, W. Zhang, B. Wang, G.A. Sewvandi, D. Yang, D. Hu, Additive manufacturing of piezoelectric materials, Adv. Funct. Mater. 30 (52) (2020) 2005141, https://doi.org/10.1002/adfm.202005141.
- [6] H. Cui, R. Hensleigh, D. Yao, D. Maurya, P. Kumar, M.G. Kang, S. Priya, X. Zheng, Three-dimensional printing of piezoelectric materials with designed anisotropy and directional response, Nat. Mater. 18 (3) (2019) 234–241, https://doi.org/10.1038/ s41563-018-0268-1.
- [7] X. Song, L. He, W. Yang, Z. Wang, Z. Chen, J. Guo, H. Wang, L. Chen, Additive manufacturing of bi-continuous piezocomposites with triply periodic phase interfaces for combined flexibility and piezoelectricity, J. Manuf. Sci. Eng. 141 (11) (2019), https://doi.org/10.1115/1.4044708.
- [8] L. He, F. Fei, W. Wang, X. Song, Support-free ceramic stereolithography of complex overhanging structures based on an elasto-viscoplastic suspension feedstock, ACS Appl. Mater. Interfaces 11 (20) (2019) 18849–18857, https://doi.org/10.1021/ acsami.9b04205.
- [9] L. He, X. Song, Supportability of a high-yield-stress slurry in a new stereolithography-based ceramic fabrication process, Jom 70 (3) (2018) 407–412, https://doi.org/10.1007/s11837-017-2657-3.
- [10] K.-H. Yoon, J. Kim, K. Jo, Dielectric properties of barium titanate with Sb2O3 and ZnO, J. Mater. Sci. Lett. 8 (2) (1989) 153–156, https://doi.org/10.1007/ bf00730709.
- [11] T.R. Armstrong, R.C. Buchanan, Influence of core-shell grains on the internal stress state and permittivity response of zirconia-modified barium titanate, J. Am. Ceram. Soc. 73 (5) (1990) 1268–1273, https://doi.org/10.1111/j.1151-2916.1990. tb05190.x.
- [12] T.R. Armstrong, L.E. Morgens, A.K. Maurice, R.C. Buchanan, Effects of zirconia on microstructure and dielectric properties of barium titanate ceramics, J. Am. Ceram. Soc. 72 (4) (1989) 605–611, https://doi.org/10.1111/j.1151-2916.1989.tb06182.
- [13] W. Kingery, B. Francis, Grain growth in porous compacts, J. Am. Ceram. Soc. 48 (10) (1965) 546–547, https://doi.org/10.1111/j.1151-2916.1965.tb14665.x.

- [14] H. Takahashi, Y. Numamoto, J. Tani, S. Tsurekawa, Piezoelectric properties of BaTiO3 ceramics with high performance fabricated by microwave sintering, Jpn. J. Appl. Phys. 45 (98) (2006) 7405–7408, https://doi.org/10.1143/JJAP.45.7405.
- [15] N. Klein, E. Hollenstein, D. Damjanovic, H. Trodahl, N. Setter, M. Kuball, A study of the phase diagram of (K, Na, Li) Nb O 3 determined by dielectric and piezoelectric measurements, and Raman spectroscopy, J. Appl. Phys. 102 (1) (2007), 014112, https://doi.org/10.1063/1.2752799.
- [16] S. Zamir, The influence of cation additives on grain-boundary mobility in yttrium aluminum garnet (YAG), J. Am. Ceram. Soc. 98 (1) (2015) 324–330, https://doi. org/10.1111/jace.13290.
- [17] K. Bodišová, D. Galusek, P. Švančárek, V. Pouchlý, K. Maca, Grain growth suppression in alumina via doping and two-step sintering, Ceram. Int. 41 (9) (2015) 11975–11983, https://doi.org/10.1016/j.ceramint.2015.05.162.
- [18] J. Schindelin, I. Arganda-Carreras, E. Frise, V. Kaynig, M. Longair, T. Pietzsch, S. Preibisch, C. Rueden, S. Saalfeld, B. Schmid, Fiji: an open-source platform for biological-image analysis, Nat. Methods 9 (7) (2012) 676–682, https://doi.org/ 10.1038/mmeth.2019.
- [19] Z. Chen, X. Song, L. Lei, X. Chen, C. Fei, C.T. Chiu, X. Qian, T. Ma, Y. Yang, K. Shung, 3D printing of piezoelectric element for energy focusing and ultrasonic sensing, Nano Energy 27 (2016) 78–86, https://doi.org/10.1016/j. pages 2016 06 048
- [20] X. Song, Y. Chen, T.W. Lee, S. Wu, L. Cheng, Ceramic fabrication using Mask-Image-Projection-based Stereolithography integrated with tape-casting, J. Manuf. Process. 20 (2015) 456–464, https://doi.org/10.1016/j.jmapro.2015.06.022.
- [21] C. Dai, C.C. Wang, C. Wu, S. Lefebvre, G. Fang, Y.-J. Liu, Support-free volume printing by multi-axis motion, ACM Trans. Graph. (TOG) 37 (4) (2018) 1–14, https://doi.org/10.1145/3197517.3201342.
- [22] A.M. Mirzendehdel, K. Suresh, Support structure constrained topology optimization for additive manufacturing, Comput. Aided Des. 81 (2016) 1–13, https://doi.org/10.1016/j.cad.2016.08.006.
- [23] J.W. Halloran, Ceramic stereolithography: additive manufacturing for ceramics by photopolymerization, Annu. Rev. Mater. Res. 46 (2016) 19–40, https://doi.org/ 10.1146/annurev-matsci-070115-031841.
- [24] J.-W. Choi, H.-C. Kim, R. Wicker, Multi-material stereolithography, J. Mater. Process. Technol. 211 (3) (2011) 318–328, https://doi.org/10.1016/j. imatprotec.2010.10.003.
- [25] C. Zhou, Y. Chen, Z. Yang, B. Khoshnevis, Digital material fabrication using mask-image-projection-based stereolithography, Rapid Prototyp. J. 19 (3) (2013) 153–165, https://doi.org/10.1108/13552541311312148. ISSN: 1355-2546, 1758-7670.
- [26] R.A. Islam, S. Priya, Realization of high-energy density polycrystalline piezoelectric ceramics, Appl. Phys. Lett. 88 (3) (2006), 032903, https://doi.org/ 10.1063/1.2166201.

- [27] J. Ryu, A.V. Carazo, K. Uchino, H.-E. Kim, Magnetoelectric properties in piezoelectric and magnetostrictive laminate composites, Jpn. J. Appl. Phys. 40 (8R) (2001) 4948–4951, https://doi.org/10.1143/JJAP.40.4948.
- [28] A. Morel, G. Pillonnet, Y. Wanderoild, A. Badel, Dielectric losses considerations for piezoelectric energy harvesting, J. Low Power Electron. 14 (2) (2018) 244–254, https://doi.org/10.1166/jolpe.2018.1562.
- [29] G. Panomsuwan, H. Manuspiya, A comparative study of dielectric and ferroelectric properties of sol-gel-derived BaTiO 3 bulk ceramics with fine and coarse grains, Appl. Phys. A 124 (10) (2018) 1–8, https://doi.org/10.1007/s00339-018-2126-z.
- [30] J.-H. Kim, W.-S. Jung, H.-T. Kim, D.-H. Yoon, Properties of BaTiO3 synthesized from barium titanyl oxalate, Ceram. Int. 35 (6) (2009) 2337–2342, https://doi. org/10.1016/j.ceramint.2009.01.006.
- [31] W.-S. Jung, J. Park, Y. Park, D.-H. Yoon, Effects of impurities on the properties of BaTiO3 synthesized from barium titanyl oxalate, Ceram. Int. 36 (6) (2010) 1997–2002, https://doi.org/10.1016/j.ceramint.2010.03.033.
- [32] A.C. Caballero, J.F. Fernández, C. Moure, P. Durán, Y.M. Chiang, Grain growth control and dopant distribution in ZnO-doped BaTiO3, J. Am. Ceram. Soc. 81 (4) (1998) 939–944, https://doi.org/10.1111/j.1151-2916.1998.tb02430.x.
- [33] M. Hasan, K. Shorowordi, Structure and dielectric properties of pure and zinc oxide-doped barium titanate, Mater. Perform. Charact. 2 (1) (2013) 174–182, https://doi.org/10.1520/MPC20130001.
- [34] J. Deng, A phase field model of sintering with direction-dependent diffusion, Mater. Trans. 53 (2) (2012) 385–389, https://doi.org/10.2320/matertrans. M2011317
- [35] K. Ahmed, C. Yablinsky, A. Schulte, T. Allen, A. El-Azab, Phase field modeling of the effect of porosity on grain growth kinetics in polycrystalline ceramics, Model. Simul. Mater. Sci. Eng. 21 (6) (2013), 065005, https://doi.org/10.1088/0965-0393/21/6/065005.
- [36] S. Biswas, D. Schwen, J. Singh, V. Tomar, A study of the evolution of microstructure and consolidation kinetics during sintering using a phase field modeling based approach, Extrem. Mech. Lett. 7 (2016) 78–89, https://doi.org/ 10.1016/j.eml.2016.02.017.
- [37] D. Zhang, Ga Weng, S. Gong, D. Zhou, The kinetics of initial stage in sintering process of BaTiO3-based PTCR ceramics and its computer simulation, Mater. Sci. Eng. B 99 (1–3) (2003) 88–92, https://doi.org/10.1016/S0921-5107(02)00426-9.
- [38] Y.U. Wang, Computer modeling and simulation of solid-state sintering: a phase field approach, Acta Mater. 54 (4) (2006) 953–961, https://doi.org/10.1016/j. actamat.2005.10.032.
- [39] N. Moelans, B. Blanpain, P. Wollants, Quantitative analysis of grain boundary properties in a generalized phase field model for grain growth in anisotropic systems, Phys. Rev. B 78 (2) (2008), 024113, https://doi.org/10.1103/ physrevb.78.024113.